Unsupervised Rapid Flood Mapping Using Sentinel-1 GRD SAR Images

Donato Amitrano, Gerardo Di Martino, *Senior Member, IEEE*,
Antonio Iodice, *Senior Member, IEEE*, Daniele Riccio, *Fellow, IEEE*,
and Giuseppe Ruello, *Member, IEEE*

Abstract—We present a new methodology for rapid flood mapping exploiting Sentinel-1 synthetic aperture radar data. In particular, we propose the usage of ground range detected (GRD) images, i.e., preprocessed products made available by the European Space Agency, which can be quickly treated for information extraction through simple and poorly demanding algorithms. The proposed framework is based on two processing levels providing event maps with increasing resolution. The first level exploits classic co-occurrence texture measures combined with amplitude information in a fuzzy classification system avoiding the critical step of thresholding. The second level consists of a change-detection approach applied to the full resolution GRD product. The discussion is supported by several experiments demonstrating the potentiality of the proposed methodology, which is particularly oriented toward the end-user community.

Index Terms—Classification, co-occurrence texture, flooding, fuzzy systems, synthetic aperture radar (SAR).

I. INTRODUCTION

EFFECTIVE response to natural disasters requires the availability of systems providing decision makers and first responders a map of the affected area in a short time [1], [2]. Floods are among the most serious natural hazards in the world, causing significant damage to people, infrastructure, and economies. This is true not only for developing countries. In fact, as an example, the U.S. Department of Commerce, National Oceanic and Atmospheric Administration estimated that in the U.S. an average of more than 225 people were killed and more than 3.5 billion dollars in property were damaged by heavy rainfall and flooding each year between 1993 and 1999 [3]. In Pakistan, between 1947 and 2008, floods in the Indus river basin claimed more than 7000 lives, inundating 7.7 million acres and causing massive infrastructure and crop losses [4]. In these scenarios, rapid estimation of inundated areas is crucial to effectively organize response operations. Emergency managers require timely information about areas interested by floodwater in order to establish interventions priority and plan mitigation measures.

The use of synthetic aperture radar (SAR) sensors is a crucial value-added in rapid mapping of flooding due to their all-weather and all-time imaging characteristics, ensuring the availability of the acquisition independently of illumination and weather conditions. However, the handling of radar data for information extraction is typically considered more difficult by end users, which often find more attractive images acquired by multispectral sensors. This is due to both interpretation and processing issues [5], the latter principally related to the possibility to operate with radiometric indices, allowing for the identification of many scene features through simple thresholding. In the case of surface water, the normalized difference water index introduced by McFeeters [6] is a tool widely employed in applications providing easily comprehensible information even for nonexpert remote sensing users [7]–[12].

However, despite their ease of use, multispectral data are often not suitable for emergency due to their sensitivity to weather and illumination conditions. Therefore, the scientific community deeply investigated the use of SAR data. Thresholding-based methods have been proposed, as an example, in [13]–[15]. Boni *et al.* [16] proposed an integrated system for flood monitoring based on the exploitation of satellite acquisitions and flood forecasts. Garcia-Pintado *et al.* [17] introduced a flood forecasting system supported by satellite SAR acquisitions. D'Addabbo *et al.* [18] presented a Bayesian network to integrate multitemporal SAR data with geomorphic and other ground information. The use of both supervised and unsupervised methods and multimodal data is investigated in [19]. Reference [20] presented a fully automated service for flood mapping exploiting TerraSAR-X data in which preprocessing, unsupervised initialization of the classification as well as postclassification refinement is automatically triggered after satellite data delivery. A method for the estimation of flood depth based on the inversion of theoretical urban scattering models was presented in [21]. Reference [22] proposed an approach exploiting TerraSAR-X data in combination with rule-based classification and Taguchi optimization techniques. Change-detection for flooding mapping in urban areas was faced in [23]. Reference [24] introduced an automatic split-based thresholding process as a computationally efficient method providing reliable results in near-real-
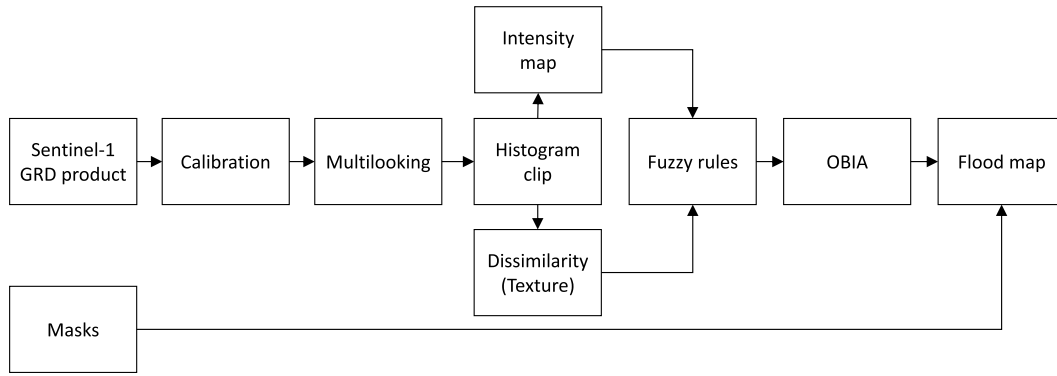
Fig. 1. RFP-L1 general workflow. The input is a calibrated Sentinel-1 GRD product with 10-m spatial resolution. It is treated with spatial multilooking for speckle reduction. Histogram clipping is then performed in order to enhance the information of low reflectivity areas. The Haralick dissimilarity texture and the reflectivity map feed a fuzzy system assigning the class "Flood" only to pixels having the characteristics required basing on the available layers. The output flood map has 30-m spatial resolution due to the applied multilook. The method is fully unsupervised and threshold-free.

time mapping. Martinis *et al.* [25] compared four operational SAR-based flood detection approaches. As for global-scale applications, an automated water mapping algorithm based on long-term training data sets to estimate the probability that a pixel is covered by water given its backscatter and incidence angle was introduced in [26].

The variety and the volume of the literature addressing floods testify that mapping surface water from space using SAR data is still an open problem. In this paper, we propose a new unsupervised framework for rapid flood mapping exploiting Sentinel-1 ground range detected (GRD) products. GRD products are detected images, made available by the European Space Agency (ESA) through the Sentinels Data Hub, on which a basic preprocessing [27] has been already implemented. Therefore, they are ready to feed information extraction processing chains.

This paper introduces a double innovation. The first one is at product level. In fact, as far we know, there are very few papers discussing the usage of Sentinel-1 GRD products in applications (see [28]–[30] for flooding application), despite they are raising more and more interest among end users being available for cloud processing within the Google Earth Engine platform [31], [32]. The second innovation is methodological. We propose two processing levels with increasing computational burden providing maps with increasing resolution. The first one is based on the analysis of the single GRD product, and basically exploits classic Haralick textural features [33]. The output is a flood map with 30-m spatial resolution obtainable with few minutes processing time on standard machines. The second processing level is based on change detection, exploiting the comparison between two GRD products imaging the same area. The output is a flood map with the same resolution of the input products, unless losses due to despeckling. In this case, the processing time varies depending on the technique selected for despeckling, which represents the most computationally demanding step of the designed chain.

This paper is organized as follows. In Section II, the proposed methodology is introduced. Experiments on five test

sites are discussed in Section III. The obtained results are compared with those given by popular classification methods in Section IV. The sensitivity of the method with respect to its parameters is explored in Section V. Conclusions are drawn at the end of this paper.

II. METHODOLOGY

The proposed methodology consists in two processing levels with increasing complexity and computational burden. In the following, we will refer to them as Level-1 rapid flood processor (RFP-L1) and Level-2 rapid flood processor (RFP-L2), respectively.

A. RFP-L1 Chain

The RFP-L1 chain is depicted in Fig. 1. The input is a calibrated Sentinel-1 GRD product (10-m spatial resolution). It is treated with a moderate multilook (3×3) in order to reduce speckle without degrading excessively the image resolution that passes from 10 to 30 m. Calibration is implemented using the *snap* platform.

After multilooking, the SAR dynamic range is reduced to compensate the presence of highly reflecting targets, resulting in an exponential probability distribution function (pdf). As suggested in [34] and [35], this can be done with a histogram clipping, which allows for relaxing the pdf, thus enhancing the information content of low reflectivity areas.

Texture processing consists in the calculation of classic Haralick features [33]. Actually, just one of them (the dissimilarity) is considered in this paper. The choice of the dissimilarity was mainly empirical. We tested different texture measures, and the best results were obtained using the dissimilarity. However, good performances, only slightly worse than those here presented, can be obtained using the homogeneity or the contrast. The adopted window dimension for texture calculation was 5 pixels in order to optimize the tradeoff between computational time (increasing with the window dimensions), robustness to outliers, and edge preservation.
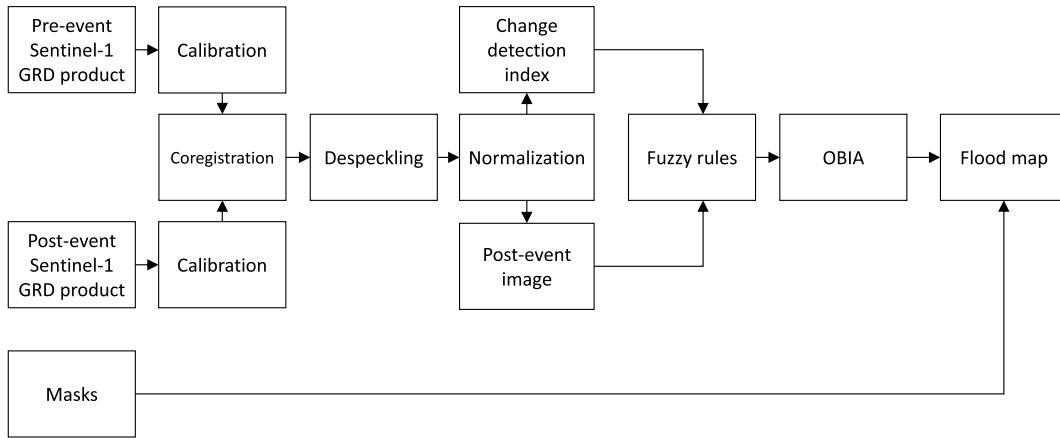
Fig. 2. RFP-L2 general workflow. The input is a couple of calibrated, coregistered Sentinel-1 GRD products with 10-m spatial resolution (preevent and postevent images). They are treated with despeckling and cross calibrated using the variable amplitude-level equalization method. A change index is defined to feed, together with the postevent image, a fuzzy system assigning the class "Flood" only to pixels having the characteristics required basing on the available layers. The output flood map has about 10-m spatial resolution (losses can occur depending on the applied despeckling). The method is fully unsupervised and threshold-free.

TABLE I

ADOPTED PARAMETERS TO MODEL THE FUZZY SETS RELEVANT TO THE SIMILARITY [SEE (1)] AND TO THE NORMALIZED GRD PRODUCT TREATED WITH MULTILOOK AND HISTOGRAM CLIPPING

Layer	Semantic attribute	Fuzzy set	a	c
Similarity	Low	Z-type	0	0.6
Similarity	High	S-type	0.5	0.7
GRD product	Low	Z-type	0	0.2
GRD product	High	S-type	0.1	0.3

TABLE II

SUMMARY OF THE AVAILABLE DATA

Dataset	Event	EMSR Code	Acquisition	Ground truth Sensor	Date
Parachique	22/03/2017	EMSR199	23/03/2017	COSMO-SkyMed	30/03/2017
Ballinasloe	08/01/2016	EMSR149	09/01/2016	Radarsat-2	11/01/2016
Selby	27/12/2015	EMSR150	01/01/2016	COSMO-SkyMed	31/12/2015
Poplar Bluff	28/04/2017	EMSR176	28/04/2017	COSMO-SkyMed	03/05/2017
Jemalong	24/09/2016	EMSR184	27/09/2016	Sentinel-1	29/09/2016

The clipped multilook product and the dissimilarity map are normalized with respect to their maximum. These two maps, ranging in the interval [0, 1], feed the fuzzy system for the extraction of the flooded area. Actually, the dissimilarity is used with its complementary to 1, that we call, for the sake of simplicity, similarity, which is defined as follows:

$$s = 1 - \hat{d} \qquad (1)$$

in which $\hat{d}$ is the normalized Haralick dissimilarity.

The two variables are modeled with two semantic attributes, "Low" and "High," corresponding to a Z-type and to an S-type fuzzy set, respectively. The fuzzy set parameters are reported in Table I. The flooded area is required to exhibit "High" similarity (since negligible texture is expected on water surfaces) and "Low" intensity.

The adoption of a fuzzy decision rule avoids the search for a threshold. In fact, the classes "Flood" and "No flood" are automatically assigned through defuzzification of the probability maps created by the fuzzy system. This step is implemented with the maximum membership method [36].

Object-based image analysis (OBIA) [37] is used to exclude from the final map all the regions whose area is smaller than a user-defined threshold. In this paper, this parameter was set to $10E^5$ m^2. OBIA processing is based on connected component labeling [38], which allows for quickly segmenting the binary images.

Permanent hydrography (rivers and lakes) and sea surfaces must be masked out from the flood map using some available ground truths. The output map has 30-m spatial resolution due to the applied multilooking. The method is fully unsupervised. Its processing time is in the order of 20 min on a 4-core, 32-GB RAM machine.

B. RFP-L2 Chain

The RFP-L2 chain is depicted in Fig. 2. The input is a couple of calibrated Sentinel-1 GRD products representing the preevent and the postevent scene situation. Calibration and coregistration are implemented using the *snap* platform.

Despeckling is crucial to enhance the contrast between water and land features. The higher the performance of the selected algorithm, the higher the quality of the output map. However, computational time will be typically higher as well. In the experiments discussed in Section III, we used a very simple despeckling algorithm, i.e., the refined-Lee filter [39], in order to optimize computational time on the available machine. However, if better performing machines are available, the usage of more aggressive and computationally demanding filters can be considered to increase the equivalent number of looks in homogeneous areas [40]–[42].

Filtered images are then subjected to cross calibration using the variable amplitude-level equalization introduced in [34] in order to ensure that the same object in different images exhibits

the same reflectivity. Cross-calibrated images are then used to compute a change index, which, following the guidelines given in [43], is formulated as follows:

$$\text{CI} = \frac{I_{t_2} - I_{t_1}}{I_{t_2} + I_{t_1}}, \quad \text{CI} \in [-1, 1] \tag{2}$$

where I_{t_2} and I_{t_1} are the preevent and postevent images, respectively.

The change index CI and the postevent image feed the fuzzy classification system. Even in this case, the two variables are modeled with the semantic attributes "Low" and "High," whose parameters are reported in Table I (for the change index, they coincide with those defined for the similarity). The flooded area should exhibit "High" change index and "Low" intensity.

At the end of the processing chain, the OBIA is used to discard regions smaller than a user-defined threshold ($5E^4$ m^2 for the RFP-L2) and to fill small holes into the retrieved map. Available ground truth about permanent hydrography is useful to reduce false alarms (FA). The output map has nominally 10-m resolution. However, losses are possible due to despeckling. The method is fully unsupervised, and its processing time (about 1.5 h using the same machine exploited to run the RFP-L1 experiments) mainly depends on the complexity of despeckling and the dimension of the input images (about 1.6 GB).

III. Experiments

The proposed methodology has been tested using five cases taken from the list of activations of the Copernicus Emergency Management Service (EMS) [44]. It is a wide repository in which both processed maps and vector ground truth can be downloaded for free. In particular, we considered the following test sites (see also Table II).

1) *Parachique (EMS Activation Code: EMSR199):* This flood, occurred on March 22, 2017, interested a wide rural region (about 33 250 ha) in the area of Parachique (Peru). The ground truth provided by the ESA is derived from a COSMO-SkyMed acquisition made on March 30, 2017 using a semiautomatic method. The image used, in this paper, for mapping the flooded area has been acquired on March 23, 2017.

2) *Selby (EMS Activation Code: EMSR150):* Severe weather and heavy rain caused flooding in the Yorkshire area (U.K.) at the end of 2015. The affected areas are those of York and Selby along the River Ouse and a large West Yorkshire zone along the Calder and Aire rivers, including the cities of Bradford and Leeds. This data set concerns the city of Selby. The image used for generating the flood map has been acquired on January 1, 2016. Ground-truth data available from the ESA were derived from a COSMO-SkyMed acquisition made on December 31, 2015, using a semiautomatic method.

3) *Ballinasloe (EMS Activation Code: EMSR149):* Heavy rain caused flooding in the central area of Ireland in January 2016. This data set concerns the city of Ballinasloe, which was one of the most affected by the event

occurred on January 8, 2016. The image used for flood mapping has been acquired on January 9, 2016. Ground-truth data available from the ESA were obtained using a semiautomatic approach applied to Radarsat-2 data acquired on January 11, 2016.

4) *Poplar Bluff (EMS Activation Code: EMSR176):* Strong storms with heavy rains affected the central U.S. at the end of April 2017 causing massive floods in Oklahoma, Arkansas, Kansas, and Missouri. This data set concerns the area surrounding the city of Poplar Bluff, MO, USA. The image used for flood mapping has been acquired on April 28, 2017. Ground-truth data made available by the ESA were retrieved using a semiautomatic method applied to COSMO-SkyMed data acquired on May 03, 2017.

5) *Jemalong (EMS Activation Code: EMSR184):* In September 2016, heavy rains hit South Eastern Australia causing flooding around the Lachlan River affecting an area of approximately 34 000 km^2. This data set concerns the city of Jemalong. The ground truth provided by the ESA is derived from a Sentinel-1 image acquired on September 29, 2016 and produced with a semiautomatic method. The image used, in this paper, to retrieve the flood map was acquired on September 27, 2016, in the descending orbit. We did not use the same image exploited by the ESA to generate the ground truth, because it seems that there are no other images acquired before September 29, 2016, in the ascending orbit along the track 155 on this site, thus making it impossible the implementation of the change detection.

In Fig. 3, we reported some pictures relevant to the RFP-L1 chain applied to two of the considered test sites (Parachique and Jemalong). In particular, the input products are shown in the first column of the picture. In the second column, the dissimilarity maps are reported. In the third column, the ground truth provided by the ESA is displayed. Flooded areas are superimposed (in cyan color) to the input products in the first column. The first row of the picture concerns the Parachique test site. The second row of the picture concerns the Jemalong test site.

The masks relevant to the permanent hydrography provided by the ESA concern the same area of the ground truth. For this reason, it is possible that lakes and rivers outside it appear in the flooding map. However, this problem can be easily solved by using a more extended database of permanent water surfaces.

The results obtained using the RFP-L1 are reported in the second and third columns of Table III. As for the detection rate (DR) with respect to the available ground truth, the following values were obtained: Parachique—99.8%, Ballinasloe—98.0%, Selby—92.1%, Poplar Bluff—96.2%, and Jemalong—91.2%. On average, the accuracy is 95.4%.

As for FA, the following values were obtained: Parachique—8.58%, Ballinasloe—4.69%, Selby—1.00%, Poplar Bluff—7.33%, and Jemalong—13.3%. The average value is 6.98%.

In Fig. 4, some pictures concerning the application of the RFP-L2 chain to the available data sets are reported.
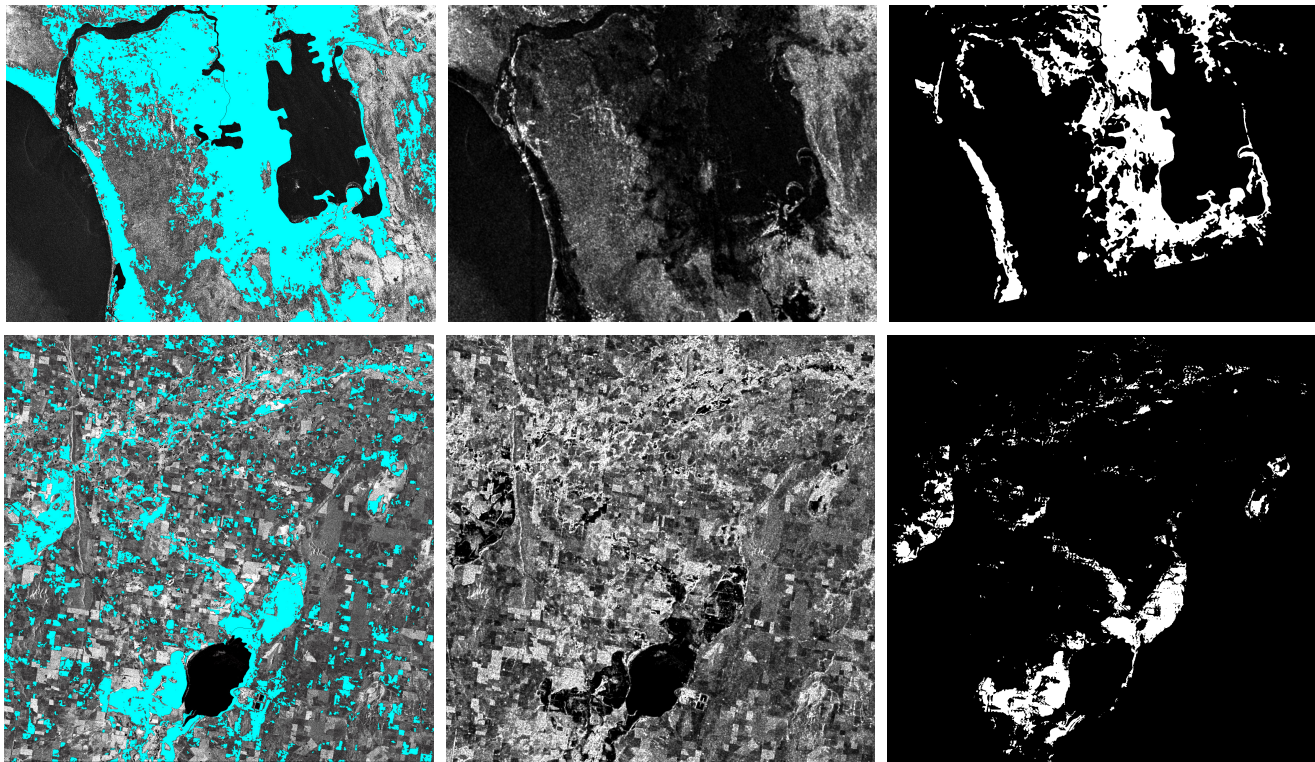
Fig. 3. RFP-L1 processing chain. First column: input GRD products (flooded areas superimposed in cyan color). Second column: dissimilarity maps. Third column: ground-truth data provided by the ESA. First row: Parachique. Second row: Jemalong.

In particular, postevent images are shown in the first column of the picture. In the second column, the change index maps [see (2)] are reported. In the third column, the ground-truth maps provided by the ESA are displayed. Flooded areas are superimposed (in cyan color) to the postevent images in the first column. The first row of the picture concerns the Ballinasloe test site. The second row of the picture concerns the Selby test site. The third row of the picture concerns the Poplar Bluff test site.

The results obtained using the RFP-L2 are reported in the second and third columns of Table IV. As for the DR with respect to the available ground truth, the following values were obtained: Parachique—97.3%, Ballinasloe—98.6%, Selby—91.8%, Poplar Bluff—84.1%, and Jemalong—93.6%. On average, the accuracy is 92.9%.

As for FA, the following values were obtained: Parachique—12.5%, Ballinasloe—6.60%, Selby—2.40%, Poplar Bluff—11.1%, and Jemalong—12.3%. The average value is 8.88%.

In general, both the RFP-L1 and RFP-L2 chains performed quite well in all the considered test cases providing high-accuracy flooding maps with rather limited occurrence of FA.

IV. COMPARISON WITH OTHER METHODS

A. Level-1 Processing

In this section, we compare the results obtained with the RFP-L1 with other popular literature methods for SAR image classification. In particular, supervised support vec-

tor machine (SVM) [45], neural net (NN) [46], maximum likelihood (ML) [46], and unsupervised k-mean were considered. Moreover, threshold-based segmentation was also experimented. In this case, the threshold was determined with supervision following the approach suggested, as an example, in [20] and [47]. The method consists in the selection of some patches relevant to a flooded area, and then computing automatically the threshold using, as suggested in [20], the minimum error algorithm [48]. The global threshold is then obtained by averaging the local thresholds found using the patches.

The results of the comparison are shown in Table III. The proposed RFP-L1 chain is able to outperform the considered literature method in terms of DR in all the considered study cases. On average, the obtained results are the following: RFP-L1—95.4%, k-mean—83.8%, SVM—82.8%, NN—57.2%, ML—51.8%, and Thresholding—66.8%.

As for FA, the best performance (on average) is given by thresholding classification. In particular, we obtained the following mean results: RFP-L1—6.98%, k-mean—22.3%, SVM—9.88%, NN—6.88 %, ML—4.94%, and Thresholding—3.95%. However, the proposed methodology offers the best tradeoff between flooding mapping accuracy and occurrence of FA. In fact, the registered value for FA is on average about 2% higher than the best performing algorithm, while the overall accuracy is, on average, at least higher than 10% with respect to the considered literature methods.

In summary, from the performed experiments, it arises that the proposed methodology gives the best tradeoff between DR

This article has been accepted for inclusion in a future issue of this journal. Content is final as presented, with the exception of pagination.

6   IEEE TRANSACTIONS ON GEOSCIENCE AND REMOTE SENSING
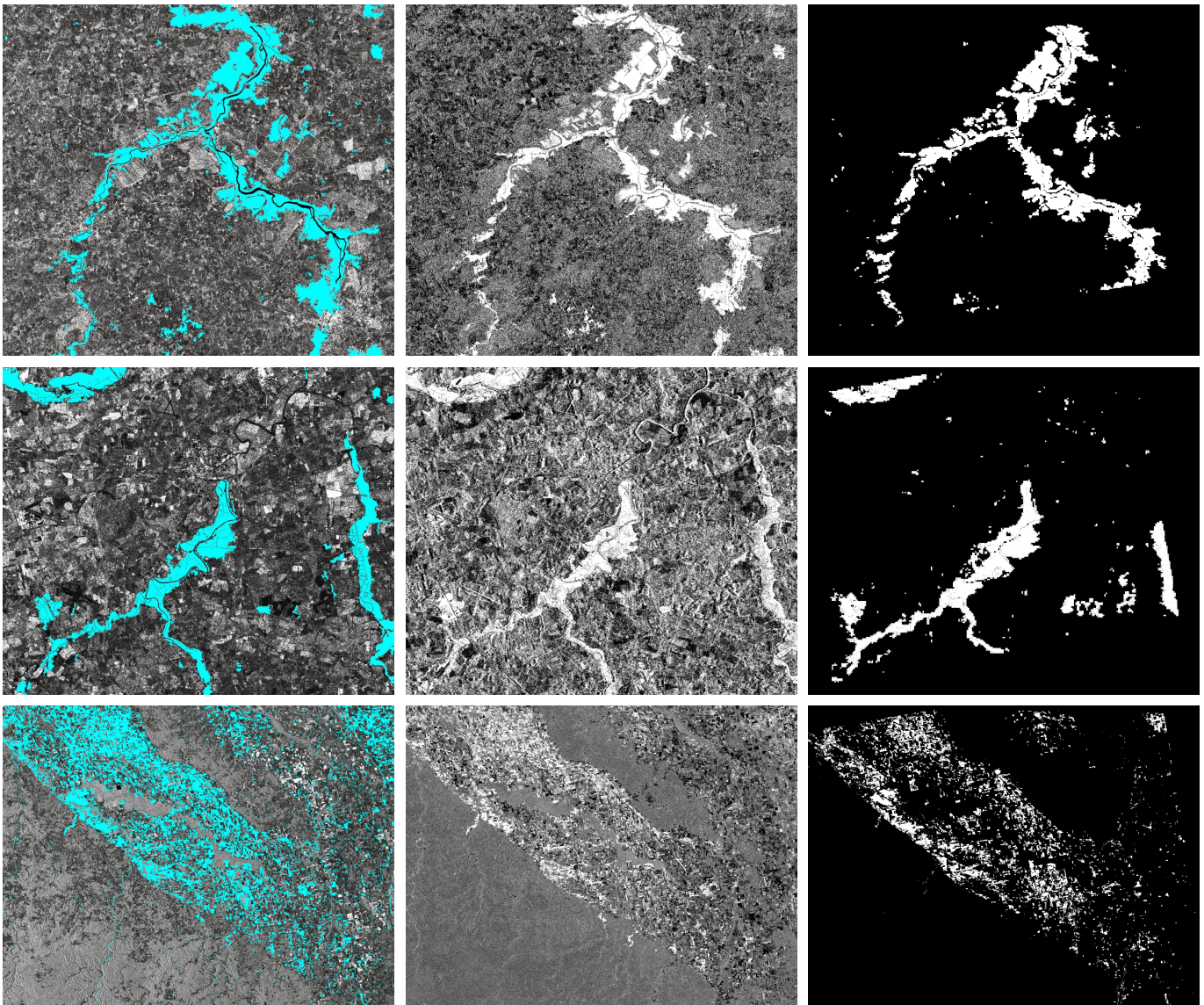

Fig. 4.   RFP-L2 processing chain. First column: input GRD products (flooded areas superimposed in cyan color). Second column: change index map. Third column: ground-truth data provided by the ESA. First row: Ballinasloe. Second row: Selby. Third row: Poplar Bluff.

and FA with respect to the tested literature methods. Further advantages are:

1) The lack of any supervision, which can significantly influence supervised classifiers due to nonoptimal selection of the relevant training samples.
2) The lack of any thresholding, thanks to the adoption of a fuzzy system combining the available layers in such a way to optimize the management of uncertainty. Local thresholding methods, in fact, although ensuring the convergence of the most popular histogram-based thresholding algorithm, can lead to overestimation/underestimation of the optimal threshold due to: 1) local variation of the backscattering (as an example, due to wind-induced surface water roughness) and 2) near-range/far-range reflectivity alteration, which is particularly critical when data are acquired in ScanSAR mode, like in the case of Sentinel-1 sensor.

Due to its characteristics, the method is particularly oriented toward end users. In fact, it does not require particular exper-

tise in remote sensing to be effectively handled. Moreover, assuming to fix the parameters ruling the fuzzy classification system (whose sensitivity is analyzed in Section V), the algorithm is practically parameter-free, since the variation of the settings illustrated in Section II is expected to have a negligible impact on the output (see Section V for details).

B. Level-2 Processing

In this section, we compare the results obtained with the RFP-L2 with other popular literature classification methods, such as SVM, NN, ML, and k-mean. Threshold-based segmentation applied both on the ratio image and the difference image (as suggested in [49]) was also implemented. In these experiments, the threshold was determined applying the same procedure used for the single GRD product.

The results of the comparison are shown in Table IV. It arises that the RFP-L2 method is able to outperform the considered literature methods in terms of DR in four cases over five. On average, the obtained results are the following: RFP-L2—92.9%, k-mean—73%, SVM—73.4%,

TABLE III
COMPARISON BETWEEN RFP-L1 AND OTHER LITERATURE CLASSIFICATION METHOD: k-MEAN, SVM, NN, ML, AND THRESHOLDING.
DR: DETECTION RATE (PERCENTAGE). FA: FALSE ALARMS (PERCENTAGE). BOLD CHARACTERS
INDICATE THE BEST REGISTERED PERFORMANCE

Dataset	Proposed		k-mean		SVM		NN		ML		Threshold	
	DR	FA	DR	FA	DR	FA	DR	FA	DR	FA	DR	FA
Parachique	**99.8**	**8.58**	97.9	44.8	99.2	33.9	88.0	22.4	87.9	15.4	88.1	9.80
Ballinasloe	**94.5**	4.69	78.2	15.8	66.6	3.36	46.3	3.11	18.4	**2.31**	58.7	3.14
Selby	**92.1**	**1.00**	86.0	14.2	91.5	2.13	55.4	1.48	50.0	**1.00**	78.7	1.22
Poplar Bluff	**96.2**	7.33	91.7	15.7	92.2	5.00	62.7	3.00	67.5	1.84	63.7	**1.30**
Jemalong	**91.2**	13.3	65.4	21.0	64.6	5.00	33.6	4.44	35.6	4.33	33.1	**4.31**
Mean	**95.4**	6.98	83.8	22.3	82.8	9.88	57.2	6.88	51.8	4.94	66.9	**3.95**

TABLE IV
COMPARISON BETWEEN RFP-L2 AND OTHER LITERATURE CLASSIFICATION METHODS. SVM: SUPPORT VECTOR MACHINE. NN: NEURAL NET.
ML: MAXIMUM LIKELIHOOD. BR: BAND RATIO. DIT: DIFFERENCE IMAGE THRESHOLDING. DR: DETECTION RATE (PERCENTAGE).
FA: FALSE ALARMS (PERCENTAGE). BOLD CHARACTERS INDICATE THE BEST REGISTERED PERFORMANCE

Dataset	Proposed		k-mean		SVM		NN		ML		BR		DIT	
	DR	FA	DR	FA	DR	FA	DR	FA	DR	FA	DR	FA	DR	FA
Parachique	**97.3**	**12.5**	95.5	35.7	96.1	26.1	83.1	14.5	92.5	26.6	51.5	30.7	44.0	26.8
Ballinasloe	**98.6**	6.60	59.1	21.9	64.6	3.94	80.9	4.70	51.4	**3.88**	96.6	6.45	90.7	9.09
Selby	91.8	**2.40**	90.2	21.2	90.5	3.39	**99.8**	6.71	94.0	2.72	95.7	29.5	86.2	24.9
Poplar Bluff	**84.1**	11.1	69.6	11.4	49.0	3.53	46.8	3.76	41.0	**3.19**	49.5	6.28	31.6	10.0
Jemalong	**93.6**	12.3	49.5	9.04	66.9	**6.11**	72.6	6.62	72.0	6.57	81.3	12.4	77.9	20.7
Mean	**92.9**	8.88	73.0	19.8	73.4	8.61	76.6	**7.25**	70.2	8.59	75.0	17.0	66.1	18.3

NN—76.6%, ML—70.2%, band ratio—75.0%, and difference image thresholding—66.1%.

As for FA, the best performance (on average) is given by the NN classifier. In particular, we obtained the following mean results: RFP-L2—8.88%, k-mean—19.8%, SVM—8.61%, NN—7.25 %, ML—8.59%, band ratio—17.0%, and difference image thresholding—18.3%. However, the proposed methodology allows for keeping an FA rate rather low with no occurrence of outliers, which are registered especially in band ratio, difference image thresholding, and k-mean classifications.

As for computational burden, neglecting the time necessary to select a significant number of training samples or to find the most reliable threshold, the best performance is, of course, given by thresholding, which restitute immediately the flooded area. As for the other methods, considering the Jemalong test site, the following computational times were registered: ML—about 5 min, SVM—about 3 h, NN—about 3 h with 1000 iterations, and k-mean—about 10 min.

In summary, the considerations made for the RFP-L1 chain hold. The proposed methodology gives the best tradeoff between DR and FA with respect to the tested literature methods, introducing also advantages concerning the lack of any supervision and thresholding. Despite the first-level chain, this algorithm requires a basic understanding of SAR processing for the selection of the despeckling algorithm, in case the operator wants to modify the standard choice of the refined-Lee method.

V. SENSITIVITY ANALYSIS

In this section, we discuss the sensitivity of the proposed methodology with respect to its parameters.

We start the assessment considering variations of the fuzzy classification system. To this end, the values reported in Table I were moved up and down of $\pm5\%$ and $\pm10\%$ in order to evaluate their influence on the performance of the algorithms. The results of these experiments are reported in Table V.

In general, the behavior of the algorithm with respect to these variations is a slightly higher overall accuracy and FA rate moving up the parameters with respect to the settings reported in Table I. On the other hand, a slightly lower overall accuracy and FA rate is registered moving them down. However, no significant variation in the performance of both RFP-L1 and RFP-L2 are observed. In fact, the ranges of the DR for the RFP-L1 are the following: DR $\in [99.7, 99.9]$ for the Parachique scene, DR $\in [96.6, 98.7]$ for the Ballinasloe scene, DR $\in [86.5, 95.6]$ for the Selby scene, DR $\in [95.9, 98.9]$ for the Poplar Bluff scene, and DR $\in [88.7, 93.8]$ for the Jemalong scene. Concerning FA, the registered ranges are the following: FA $\in [7.04, 10.2]$ for the Parachique scene, FA $\in [4.46, 5.06]$ for the Ballinasloe scene, FA $\in [0.78, 1.34]$ for the Selby scene, FA $\in [6.19, 8.78]$ for the Poplar Bluff scene, and FA $\in [10.3, 13.3]$ for the Jemalong scene.

As for the RFP-L2 chain, the registered ranges for the DR are the following: DR $\in [94.8, 98.4]$ for the Parachique scene, $DR \in [98.3, 98.7]$ for the Ballinasloe scene, DR $\in [91.6, 91.9]$ for the Selby scene, DR $\in [81.0, 86.9]$ for the Poplar Bluff scene, and DR $\in [92.2, 93.5]$ for the Jemalong scene. Concerning FA, the registered ranges are the following: FA $\in [10.2, 15.0]$ for the Parachique scene, FA $\in [6.29, 7.01]$ for the Ballinasloe scene, FA $\in [2.26, 2.61]$ for the Selby scene, FA $\in [10.0, 12.3]$ for the Poplar Bluff scene, and FA $\in [11.3, 13.4]$ for the Jemalong scene.

These experiments confirm the robustness of the proposed methodology with respect to variations of the fuzzy classification parameters.

Finally, we assessed the robustness of the presented methodology with respect to the size of the texture window w,

This article has been accepted for inclusion in a future issue of this journal. Content is final as presented, with the exception of pagination.

8   IEEE TRANSACTIONS ON GEOSCIENCE AND REMOTE SENSING

TABLE V
SENSITIVITY ANALYSIS WITH RESPECT TO FUZZY SET PARAMETERS. O: "OPTIMUM" SETUP AS REPORTED IN TABLE I (BOLD CHARACTERS).
DR: DETECTION RATE (PERCENTAGE). FA: FALSE ALARMS (PERCENTAGE)

Dataset	RFP-L1										RFP-L2									
	−10%		−5%		**O**		+5%		+10%		−10%		−5%		**O**		+5%		+10%	
	DR	FA	DR	FA	DR	FA	DR	FA	DR	FA	DR	FA	DR	FA	DR	FA	DR	FA	DR	FA
Parachique	99.7	7.04	99.8	7.81	**99.8**	**8.58**	99.9	9.41	99.9	10.2	94.8	10.2	96.7	11.7	**97.3**	**12.5**	97.7	13.4	98.4	15.0
Ballinasloe	96.6	4.46	97.3	4.57	**98.0**	**4.69**	98.3	4.85	98.7	5.06	98.3	6.29	98.4	6.42	**98.6**	**6.60**	98.6	6.77	98.7	7.01
Selby	86.5	0.78	89.5	0.88	**92.1**	**1.00**	93.9	1.17	95.6	1.34	91.6	2.26	91.7	2.34	**91.8**	**2.40**	91.8	2.51	91.9	2.61
Poplar Bluff	95.9	6.19	96.7	6.80	**96.2**	**7.33**	98.4	8.09	98.9	8.78	81.0	10.0	83.0	10.6	**84.1**	**11.1**	85.2	11.6	86.9	12.3
Jemalong	88.7	10.3	89.9	11.7	**91.2**	**13.3**	92.4	14.8	93.8	16.8	92.2	11.3	92.6	11.8	**93.6**	**12.3**	93.2	12.8	92.5	13.4
Mean	93.5	5.75	96.6	6.35	**95.4**	**6.98**	96.6	7.66	97.4	8.43	91.6	8.01	92.5	8.52	**92.9**	**8.88**	93.3	9.41	93.9	10.0

TABLE VI
SENSITIVITY ANALYSIS WITH RESPECT TO VARIATIONS OF THE TEXTURE WINDOW SIZE w, OF THE HISTOGRAM CLIPPING PARAMETER k, AND OF THE
MINIMUM MAPPED AREA $\hat{A}$. DR: DETECTION RATE (PERCENTAGE). FA: FALSE ALARMS (PERCENTAGE)

Dataset	$w = 3$		$w = 7$		$\hat{A} = 5E^4$		$\hat{A} = 2E^5$		$k = 98\%$	
	DR	FA	DR	FA	DR	FA	DR	FA	DR	FA
Parachique	99.8	8.58	99.8	8.58	99.8	8.80	99.7	8.40	99.7	7.03
Ballinasloe	98.0	4.70	97.4	4.61	98.4	4.82	96.9	4.47	97.7	4.43
Selby	92.2	1.00	91.8	0.09	92.1	1.18	91.2	0.08	91.5	0.09
Poplar Bluff	96.2	7.33	96.2	7.33	96.1	7.06	93.9	6.31	95.6	6.74
Jemalong	91.2	13.3	91.1	13.3	91.6	13.9	90.7	12.7	92.2	9.71
Mean	95.5	6.98	95.2	6.78	95.6	7.15	94.5	6.39	95.3	5.60

the histogram clipping parameter k, and the minimum mapped area $\hat{A}$. We repeated the above-discussed experiments varying one parameter per time with respect to the "optimum" setup in order to evaluate the impact of each of them on the adopted quality indicators. To this end, we set $w = 3$, $w = 7$, $k = 98\%$, $\hat{A} = 5E^4$, and $\hat{A} = 2E^5$ (i.e., the minimum mapped area has been halved and doubled with respect to the "optimum" setup). The results of this assessment are presented in Table VI, in which no significant variations are appreciated with respect to the values of DR and FA reported for the "optimum" parameter setup. For brevity, we report just the results obtained for RFP-L1 chain.

VI. CONCLUSION

Rapid mapping of a flooded area is crucial for the implementation of an effective response. SAR sensors, thanks to their all-weather and all-time imaging capabilities, are a powerful instrument, able to provide timely information to first responders and decision makers. In this paper, we introduced a novel methodology for unsupervised flooding mapping exploiting preprocessed Sentinel-1 GRD products provided by the ESA through the Sentinels Data Hub. It consists of two successive processing levels with increasing computational burden, giving as output event maps with increasing resolution.

The first level accepts as input the postevent image, which is analyzed for standard Haralick textural features. Among them, the dissimilarity measure is exploited to feed, together with the amplitude information, a fuzzy classification system. The output is a map with 30-m spatial resolution due to the applied multilooking for speckle reduction. The processing time is in the order of 20 min on a standard personal computer.

The second processing level is based on change detection between a preevent and a postevent image. They are combined in a change index feeding, together with the postevent amplitude information, the fuzzy classification system. The output is a flood map having the same resolution of the input product (10 m), neglecting possible losses due to despeckling.

The processing time depends on the selected despeckling algorithm. We tested the refined-Lee algorithm obtaining satisfying results with respect to the available ground truth with a processing time of about 1.5 h for all the considered test sites. Both the level-one and level-two processing chains are fully unsupervised and threshold-free thanks to the adoption of fuzzy classification rules.

The performance of the proposed methodology was compared with those of several literature methods. As a result, we obtained that our method was able to outperform all of them providing the best tradeoff between the DR and FA.

The proposed method aims at providing end users and decision makers with a new unsupervised tool for rapid flood mapping to support the first response to this kind of events.

ACKNOWLEDGMENT

REFERENCES

[1] Y. A. Buehler, T. W. Kellenberger, D. Small, and K. I. Itten, "Rapid mapping with remote sensing data during flooding 2005 in Switzerland by object-based methods: A case study," *WIT Trans. Ecol. Environ.*, vol. 89, pp. 391–400, 2006.

[2] J. F. Rosser, D. G. Leibovici, and M. J. Jackson, "Rapid flood inundation mapping using social media, remote sensing and topographic data," *Natural Hazards*, vol. 87, no. 1, pp. 103–120, May 2017.

[3] Committee on Earth Observation Satellites, "The use of earth observing satellites for hazard support: Assessments and scenarios," U.S. Dept. Commerce, Nat. Ocean. Atmos. Admin., Silver Spring, MD, USA, Tech. Rep., 2002.

[4] M. Haq, M. Akhtar, S. Muhammad, S. Paras, and J. Rahmatullah, "Techniques of Remote Sensing and GIS for flood monitoring and damage assessment: A case study of Sindh province, Pakistan," *Egyptian J. Remote Sens. Space Sci.*, vol. 15, no. 2, pp. 135–141, Dec. 2012.

[5] D. Amitrano *et al.*, "Multitemporal level-1β products: Definitions, interpretation, and applications," *IEEE Trans. Geosci. Remote Sens.*, vol. 54, no. 11, pp. 6545–6562, Nov. 2016.

[6] S. K. McFeeters, "The use of the Normalized Difference Water Index (NDWI) in the delineation of open water features," *Int. J. Remote Sens.*, vol. 17, no. 7, pp. 1425–1432, Apr. 1996.

This article has been accepted for inclusion in a future issue of this journal. Content is final as presented, with the exception of pagination.

AMITRANO *et al.*: UNSUPERVISED RAPID FLOOD MAPPING USING SENTINEL-1 GRD SAR IMAGES 9

[7] D. A. Roshier, P. H. Whetton, R. J. Allan, and A. I. Robertson, "Distribution and persistence of temporary wetland habitats in arid Australia in relation to climate," *Austral Ecol.*, vol. 26, no. 4, pp. 371–384, Aug. 2001.

[8] A. Davranche, G. Lefebvre, and B. Poulin, "Wetland monitoring using classification trees and SPOT-5 seasonal time series," *Remote Sens. Environ.*, vol. 114, no. 3, pp. 552–562, Mar. 2010.

[9] T. Sakamoto, N. Van Nguyen, A. Kotera, H. Ohno, N. Ishitsuka, and M. Yokozawa, "Detecting temporal changes in the extent of annual flooding within the Cambodia and the Vietnamese Mekong Delta from MODIS time-series imagery," *Remote Sens. Environ.*, vol. 109, no. 3, pp. 295–313, Aug. 2007.

[10] S. K. McFeeters, "Using the Normalized Difference Water Index (NDWI) within a geographic information system to detect swimming pools for mosquito abatement: A practical approach," *Remote Sens.*, vol. 5, no. 7, pp. 3544–3561, 2013.

[11] J. C. Campos, N. Sillero, and J. C. Brito, "Normalized difference water indexes have dissimilar performances in detecting seasonal and permanent water in the Sahara–Sahel transition zone," *J. Hydrol.*, vols. 464–465, pp. 438–446, Sep. 2012.

[12] G. Donchyts, J. Schellekens, H. Winsemius, E. Eisemann, and N. van de Giesen, "A 30 m resolution surface water mask including estimation of positional and thematic differences using Landsat 8, SRTM and OpenStreetMap: A case study in the Murray-Darling basin, Australia," *Remote Sens.*, vol. 8, no. 5, p. 386, 2016.

[13] D. Amitrano *et al.*, "Modeling watershed response in semiarid regions with high-resolution synthetic aperture radars," *IEEE J. Sel. Topics Appl. Earth Observ. Remote Sens.*, vol. 7, no. 7, pp. 2732–2745, Jul. 2014.

[14] I. Heine, T. Francke, C. Rogass, P. H. A. Medeiros, A. Bronstert, and S. Foerster, "Monitoring seasonal changes in the water surface areas of reservoirs using TerraSAR-X time series data in semiarid northeastern Brazil," *IEEE J. Sel. Topics Appl. Earth Observ. Remote Sens.*, vol. 7, no. 8, pp. 3190–3199, Aug. 2014.

[15] S. Zhang, S. Foerster, P. Medeiros, J. C. de Araújo, M. Motagh, and B. Waske, "Bathymetric survey of water reservoirs in north-eastern Brazil based on TanDEM-X satellite data," *Sci. Total Environ.*, vol. 571, pp. 575–593, Nov. 2016.

[16] G. Boni *et al.*, "A prototype system for flood monitoring based on flood forecast combined with COSMO-SkyMed and sentinel-1 data," *IEEE J. Sel. Topics Appl. Earth Observ. Remote Sens.*, vol. 9, no. 6, pp. 2794–2805, Jun. 2016.

[17] J. García-Pintado *et al.*, "Satellite-supported flood forecasting in river networks: A real case study," *J. Hydrol.*, vol. 523, pp. 706–724, Apr. 2015.

[18] A. D'Addabbo, A. Refice, G. Pasquariello, F. P. Lovergine, D. Capolongo, and S. Manfreda, "A Bayesian network for flood detection combining SAR imagery and ancillary data," *IEEE Trans. Geosci. Remote Sens.*, vol. 54, no. 6, pp. 3612–3625, Jun. 2016.

[19] N. Longbotham *et al.*, "Multi-modal change detection, application to the detection of flooded areas: Outcome of the 2009–2010 data fusion contest," *IEEE J. Sel. Topics Appl. Earth Observ. Remote Sens.*, vol. 5, no. 1, pp. 331–342, Feb. 2012.

[20] S. Martinis, J. Kersten, and A. Twele, "A fully automated TerraSAR-X based flood service," *ISPRS J. Photogram. Remote Sens.*, vol. 104, pp. 203–212, Jun. 2015.

[21] P. Iervolino, R. Guida, A. Iodice, and D. Riccio, "Flooding water depth estimation with high-resolution SAR," *IEEE Trans. Geosci. Remote Sens.*, vol. 53, no. 5, pp. 2295–2307, May 2015.

[22] B. Pradhan, M. S. Tehrany, and M. N. Jebur, "A new semiautomated detection mapping of flood extent from TerraSAR-X satellite image using rule-based classification and Taguchi optimization techniques," *IEEE Trans. Geosci. Remote Sens.*, vol. 54, no. 7, pp. 4331–4342, Jul. 2016.

[23] L. Giustarini, R. Hostache, P. Matgen, G. J.-P. Schumann, P. D. Bates, and D. C. Mason, "A change detection approach to flood mapping in urban areas using TerraSAR-X," *IEEE Trans. Geosci. Remote Sens.*, vol. 51, no. 4, pp. 2417–2430, Apr. 2013.

[24] S. Martinis, A. Twele, and S. Voigt, "Towards operational near real-time flood detection using a split-based automatic thresholding procedure on high resolution TerraSAR-X data," *Natural Hazards Earth Syst. Sci.*, vol. 9, no. 2, pp. 303–314, 2009.

[25] S. Martinis *et al.*, "Comparing four operational SAR-based water and flood detection approaches," *Int. J. Remote Sens.*, vol. 36, no. 13, pp. 3519–3543, 2015.

[26] R. S. Westerhoff, M. P. H. Kleuskens, H. C. Winsemius, H. J. Huizinga, G. R. Brakenridge, and C. Bishop, "Automated global water mapping based on wide-swath orbital synthetic-aperture radar," *Hydrol. Earth Syst. Sci.*, vol. 17, pp. 651–663, Feb. 2013.

[27] F. D. Zan and A. M. M. Guarnieri, "TOPSAR: Terrain observation by progressive scans," *IEEE Trans. Geosci. Remote Sens.*, vol. 44, no. 9, pp. 2352–2360, Sep. 2006.

[28] I. Elkhrachy, "Assessment and management flash flood in Najran Wady using GIS and remote sensing," *J. Indian Soc. Remote Sens.*, pp. 1–12, May 2017.

[29] E. Psomiadis, "Flash flood area mapping utilising SENTINEL-1 radar data," *Proc. SPIE*, vol. 10005, p. 100051G, Oct. 2016.

[30] M. A. Clement, C. G. Kilsby, and P. Moore, "Multi-temporal synthetic aperture radar flood mapping using change detection," *J. Flood Risk Manage.*, pp. 1–17, 2017.

[31] N. Gorelick, M. Hancher, M. Dixon, S. Ilyushchenko, D. Thau, and R. Moore, "Google Earth Engine: Planetary-scale geospatial analysis for everyone," *Remote Sens. Environ.*, vol. 202, pp. 18–27, Dec. 2017.

[32] G. Donchyts, F. Baart, H. Winsemius, N. Gorelick, J. Kwadijk, and N. van de Giesen, "Earth's surface water change over the past 30 years," *Nature Climate Change*, vol. 6, no. 9, pp. 810–813, 2016.

[33] R. M. Haralick, K. Shanmugam, and I. H. Dinstein, "Textural features for image classification," *IEEE Trans. Syst., Man, Cybern.*, vol. SMC-3, no. 6, pp. 610–621, Nov. 1973.

[34] D. Amitrano, G. Di Martino, A. Iodice, D. Riccio, and G. Ruello, "A new framework for SAR multitemporal data RGB representation: Rationale and products," *IEEE Trans. Geosci. Remote Sens.*, vol. 53, no. 1, pp. 117–133, Jan. 2015.

[35] S. G. Dellepiane and E. Angiati, "A new method for cross-normalization and multitemporal visualization of SAR images for the detection of flooded areas," *IEEE Trans. Geosci. Remote Sens.*, vol. 50, no. 7, pp. 2765–2779, Jul. 2012.

[36] D. Amitrano *et al.*, "Urban areas enhancement in multitemporal SAR RGB images using adaptive coherence window and texture information," *IEEE J. Sel. Topics Appl. Earth Observ. Remote Sens.*, vol. 9, no. 8, pp. 3740–3752, Aug. 2016.

[37] S. Lang, "Object-based image analysis for remote sensing applications: Modeling reality—Dealing with complexity," in *Object-Based Image Analysis—Spatial Concepts for Knowledge-Driven Remote Sensing Applications*, T. Blaschke, S. Lang, and G. Hay, Eds. Berlin, Germany: Springer-Verlag, 2008, pp. 3–28.

[38] L. G. Shapiro and G. C. Stockman, *Computer Vision*. Upper Saddle River, NJ, USA: Prentice-Hall, 2002.

[39] J.-S. Lee, "Refined filtering of image noise using local statistics," *Comput. Graph. Image Process.*, vol. 15, no. 4, pp. 380–389, 1981.

[40] S. Parrilli, M. Poderico, C. V. Angelino, and L. Verdoliva, "A nonlocal SAR image denoising algorithm based on LLMMSE wavelet shrinkage," *IEEE Trans. Geosci. Remote Sens.*, vol. 50, no. 2, pp. 606–616, Feb. 2012.

[41] C.-A. Deledalle, L. Denis, and F. Tupin, "Iterative weighted maximum likelihood denoising with probabilistic patch-based weights," *IEEE Trans. Image Process.*, vol. 18, no. 12, pp. 2661–2672, Dec. 2009.

[42] Y. Yu and S. T. Acton, "Speckle reducing anisotropic diffusion," *IEEE Trans. Image Process.*, vol. 11, no. 11, pp. 1260–1270, Nov. 2002.

[43] D. Amitrano, G. D. Martino, A. Iodice, D. Riccio, and G. Ruello, "Small reservoirs extraction in semiarid regions using multitemporal synthetic aperture radar images," *IEEE J. Sel. Topics Appl. Earth Observ. Remote Sens.*, vol. 10, no. 8, pp. 3482–3492, Aug. 2017.

[44] Copernicus Emergency Management Service. *Directorate Space, Security and Migration, European Commission Joint Research Centre (EC JRC)*. Accessed: Jan. 31, 2018. [Online]. Available: http://emergency.copernicus.eu/

[45] C. J. C. Burges, "A tutorial on support vector machines for pattern recognition," in *Data Mining and Knowledge Discovery*, U. Fayyad, Ed. Norwell, MA, USA: Kluwer, 1998.

[46] J. A. Richards and X. Jia, *Remote Sensing Digital Image Analysis—An Introduction*, 4th ed. Berlin, Germany: Springer-Verlag, 2006.

[47] F. Bovolo and L. Bruzzone, "A split-based approach to unsupervised change detection in large-size multitemporal images: Application to tsunami-damage assessment," *IEEE Trans. Geosci. Remote Sens.*, vol. 45, no. 6, pp. 1658–1670, Jun. 2007.

[48] J. Kittler and J. Illingworth, "Minimum error thresholding," *Pattern Recognit.*, vol. 19, no. 1, pp. 41–47, 1986.

[49] S. Long, T. E. Fatoyinbo, and F. Policelli, "Flood extent mapping for Namibia using change detection and thresholding with SAR," *Environ. Res. Lett.*, vol. 9, no. 3, pp. 35002–35009, 2014.

This article has been accepted for inclusion in a future issue of this journal. Content is final as presented, with the exception of pagination.

10   IEEE TRANSACTIONS ON GEOSCIENCE AND REMOTE SENSING

Donato Amitrano was born in Naples, Italy, in 1985. He received the bachelor's degree in aerospace engineering, the master's degree in aerospace and astronautical engineering, and the Ph.D. degree in electronic and telecommunication engineering from the University of Naples Federico II, Naples, in 2009, 2012, and 2016, respectively.

Since 2016, he has been a Research Fellow with the University of Napoli Federico II. In 2017, he was a Co-Founder and the CEO of Latitudo 40, Naples, a high-tech company spin-off of the University of Napoli Federico II operating in the remote sensing sector. His research interests include multitemporal synthetic aperture radar (SAR), remote-sensing techniques for developing countries, machine learning, human vision, SAR images interpretation and understanding, and data fusion.

Dr. Amitrano reached the second place (in team) in the University Challenge of the ESA Copernicus Masters Competition in 2017.

Gerardo Di Martino (S'06–M'09–SM'17) was born in Naples, Italy, in 1979. He received the Laurea degree (*cum laude*) in telecommunication engineering and the Ph.D. degree in electronic and telecommunication engineering from the University Federico II, Naples, in 2005 and 2009, respectively.

From 2009 to 2016, he was with the University of Naples Federico II, where he was involved in applied electromagnetics and remote sensing topics. From 2014 to 2016, he was also with the Italian National Consortium for Telecommunications, Naples, and the Regional Center Information Communication Technology, Naples. He is currently an Assistant Professor of electromagnetics with the Department of Electrical Engineering and Information Technology, University of Naples Federico II. His research interests include microwave remote sensing and electromagnetics, with a focus on electromagnetic scattering from natural surfaces and urban areas, synthetic aperture radar (SAR) signal processing and simulation, information retrieval from SAR data, and remote sensing techniques for developing countries.

Antonio Iodice (S'97–M'00–SM'04) was born in Naples, Italy, in 1968. He received the Laurea degree (*cum laude*) in electronic engineering and the Ph.D. degree in electronic engineering and computer science from the University of Naples Federico II, Naples, in 1993 and 1999, respectively.

In 1995, he was with the Research Institute for Electromagnetism and Electronic Components, Italian National Council of Research, Naples. From 1999 to 2000, he was with Telespazio S.p.A., Rome, Italy. From 2000 to 2004, he was a Research Scientist with the Department of Electronic and Telecommunication Engineering, University of Naples Federico II. He has been a Professor of electromagnetics with the Department of Electrical Engineering and Information Technology, University of Naples Federico II, since 2005. He has been involved as a Principal Investigator or a Co-Investigator in several projects funded by the European Union, the Italian Space Agency, the Italian Ministry of Education and Research, the Campania Regional Government, and private companies. He has authored or co-authored over 300 papers, of which more than 80 published on refereed journals and the others on proceedings of international and national conferences. His research interests include microwave remote sensing and electromagnetics: modeling of electromagnetic scattering from natural surfaces and urban areas, simulation and processing of synthetic aperture radar signals, and electromagnetic propagation in urban areas.

Dr. Iodice received the 2009 Sergei A. Schelkunoff Transactions Prize Paper Award from the IEEE Antennas and Propagation Society, for the best paper published in 2008 on the IEEE TRANSACTIONS ON ANTENNAS AND PROPAGATION. He was recognized by the IEEE Geoscience and Remote Sensing Society as 2015 Best Reviewer of the IEEE TRANSACTIONS ON GEOSCIENCE AND REMOTE SENSING. He is the Chair of the IEEE South Italy Geoscience and Remote Sensing Chapter.

Daniele Riccio (M'91–SM'99–F'14) was born in Naples, Italy. He received the Laurea degree (*cum laude*) in electronic engineering from the University of Naples Federico II, Naples, in 1989.

He started his career at the University of Naples Federico II, where he is currently a Full Professor of electromagnetic fields with the Department of Electrical Engineering and Information Technology. He was a Research Scientist with the Institute for Research on Electromagnetics and Electronic Components, Italian National Research Council, from 1989 to 1994; a Guest Scientist with the German Aerospace Centre (DLR), Munich, Germany, in 1994 and 1995; a Lecturer to the Ph.D. Program with the Universitat Politecnica de Catalunya, Barcelona, Spain, in 2006, and Czech Technical University, Prague, Czech Republic, in 2012. He is a member of the Cassini Radar Science Team. He is the Coordinator of the Ph.D. School of Information Technology and Electrical Engineering, University of Napoli Federico II, where he is also a Representative of the Assembly of the National Inter-University Consortium for Telecommunications and the Scientific Board of the Italian Society of Electromagnetism. He has authored three books, including *Scattering, Natural Surfaces and Fractals* (2007), and over 400 scientific papers. His research interests include microwave remote sensing, electromagnetic scattering, synthetic aperture radar with emphasis on sensor design, data simulation and information retrieval, and application of fractal geometry to remote sensing.

Prof. Riccio was a recipient of the 2009 Sergei A. Schelkunoff Transactions Prize Paper Award for the best paper published in 2008 on the IEEE TRANS-ACTIONS ON ANTENNAS AND PROPAGATION. He serves as an associate editor for several journals on remote sensing.

Giuseppe Ruello (S'00–M'04) was born in Naples, Italy, in 1975. He received the Laurea degree (*cum laude*) in telecommunication engineering and the Ph.D. degree in information engineering from the University of Naples Federico II, Naples, in 1999 and 2003, respectively.

In 2002 and from 2004 to 2005, he was a Visiting Scientist with the Department of Signal Theory and Communications, Universitat Politecnica de Catalunya, Barcelona, Spain. He is currently a Research Scientist and an Aggregate Professor with the Department of Electrical and Information Technology Engineering, University of Naples Federico II. His research interests include synthetic aperture radar (SAR) remote sensing, modeling of electromagnetic scattering from natural surfaces, fractal models, SAR raw signal simulation, modeling of electromagnetic field propagation in urban environment, and remote sensing techniques for low-income semiarid regions.

Dr. Ruello received a grant from the University of Naples Federico II to be spent at the Department of Electronic and Telecommunication Engineering for research in remote sensing in 2000. He also received a grant from the University of Rome La Sapienza, Rome, Italy, in 2000.